Research Article | Vol. 26, No. 23 | 12 Nov 2018 | OPTICS EXPRESS 30523
Optics EXPRESS

Waveform reconstruction with a Cs based free-induction-decay magnetometer

DOMINIC HUNTER,[1,*] RICARDO JIMÉNEZ-MARTÍNEZ,[2] JUAN HERBSOMMER,[3] SRINATH RAMASWAMY,[3] WEN LI,[3] AND ERLING RIIS[1]

[1]SUPA, Department of Physics, University of Strathclyde, Glasgow G4 0NG, UK
[2]ICFO–Institut de Ciencies Fotoniques, The Barcelona Institute of Science and Technology, 08860 Castelldefels (Barcelona), Spain
[3]Texas Instruments Incorporated, 13560 N. Central Expressway, Dallas, TX 75243, USA
[*]dominic.hunter@strath.ac.uk

Abstract: We demonstrate an optically pumped magnetometer (OPM) operated in a free-induction-decay (FID) configuration that is capable of tracking oscillating magnetic signals in the presence of a 50 μT static field. Excellent waveform reconstruction is demonstrated for low frequency modulations with respect to the Nyquist limited bandwidth. A 100 pT oscillation was successfully reconstructed using signal averaging, and an optimum sensitivity of 3.9 pT/$\sqrt{\text{Hz}}$ was measured from the spectrum of the residuals relative to the sinusoidal fit. The impact of the pump-probe repetition rate and spin depolarization on the frequency response of the sensor is investigated in detail using miniaturized vapor cell technology, with the (−3 dB) bandwidths residing beyond the Nyquist limit in each case. We also discuss technical limitations associated with the magnetometer when exposed to oscillating fields of sufficiently high amplitude or frequency. This is discussed in the context of potential distortions arising in the reproduced signals, induced by frequency modulation (FM) and aliasing artefacts.

1. Introduction

Optically pumped atomic magnetometers (OPMs) employ spin-polarized alkali-metal atoms in the vapor phase as the magnetically responsive medium. Numerous OPM configurations exist in the field [1], each with their own trade-offs in terms of device performance, e.g. sensitivity, accuracy, bandwidth, dynamic range, and design simplicity [2]. This degree of flexibility is advantageous as it opens up a plethora of potential applications in areas including industrial, e.g. in maintenance of moving metallic machinery [3], medicine, e.g. detection of extremely weak fields of biological origin [4], or in fundamental research [5]. Of particular recent interest are scalar pulsed magnetometers [6, 7] in which the magnetic field is estimated directly from the frequency of the recorded free-induction-decay (FID) experienced by the spin-polarized atoms. This modality does not rely on additional hardware such as a concurrent drive, phase detection, or feedback loops to obtain the absolute strength of the magnetic field. As a result FID OPMs not only offer a simple device design but also exhibit superior accuracy compared with the commonly used driven architectures, which are prone to systematic errors due to their auxiliary instrumentation [6]. FID OPMs are now routinely used to perform DC magnetic field measurements in experiments ranging from searches for electric dipole moments (EDM) [6,8,9] to tests of quantum limits of sensing [7]. Equally attractive is their use to perform AC measurements that also benefit from miniaturized instrumentation; this regime however, has yet to be explored.

In this paper we propose and demonstrate a FID OPM capable of DC and AC measurements and exemplify its use in tracking time-varying magnetic signals in a static bias field of similar strength to that of the Earth's (~ 50 μT). Our device implements a microfabricated vapor cell [10],

#342304 https://doi.org/10.1364/OE.26.030523
Journal © 2018 Received 20 Aug 2018; revised 23 Oct 2018; accepted 23 Oct 2018; published 7 Nov 2018

Optics EXPRESS

thus is amenable for miniaturization with the added advantages of increasing spatial resolution of potential sensor networks, reducing power consumption, improving portability and lowering the cost of fabrication whilst retaining competitiveness with existing technologies [11]. Although the microfabricated nature of these vapor cells sets a fundamental limit on the optimum sensitivity achievable, it also introduces large improvements in the sensor bandwidth by virtue of the rapid spin decoherence that facilitates a quick atomic response to rapidly fluctuating fields [12]. The FID implementation is subject to certain technical limitations that are investigated in detail; for example, we assess the impacts that atomic spin relaxation and a finite detection time have on the frequency response of the device. Also, nonlinearities induced by sufficiently strong time-varying magnetic signals are observed and modelled in terms of Bessel functions of the first kind. We discuss this in the context of potential readout errors that can occur in the presence of prominent frequency modulation (FM) effects that introduce numerous frequency components into the FID spectrum. This increases the difficulty of frequency extraction using traditional digital signal processing (DSP) techniques such as discrete Fourier transforms (DFTs) or fitting algorithms, and therefore places an upper limit on the sensors dynamic range with regards to AC magnetic field perturbations that can be reliably reconstructed.

2. Principles of broadband free-induction-decay magnetometer

FID magnetometry is implemented in two sequential steps. In the first step, optical pumping, the atoms are prepared in a well-defined spin orientation through their interaction with resonant or near-resonance light. In the second step, probing, direct detection of the free evolution of the spins allows a measurement of the strength of the magnetic field **B**. The pumping and probing sequence is shown in Fig. 1 with the pump stage lasting a time interval T_p, and the detection

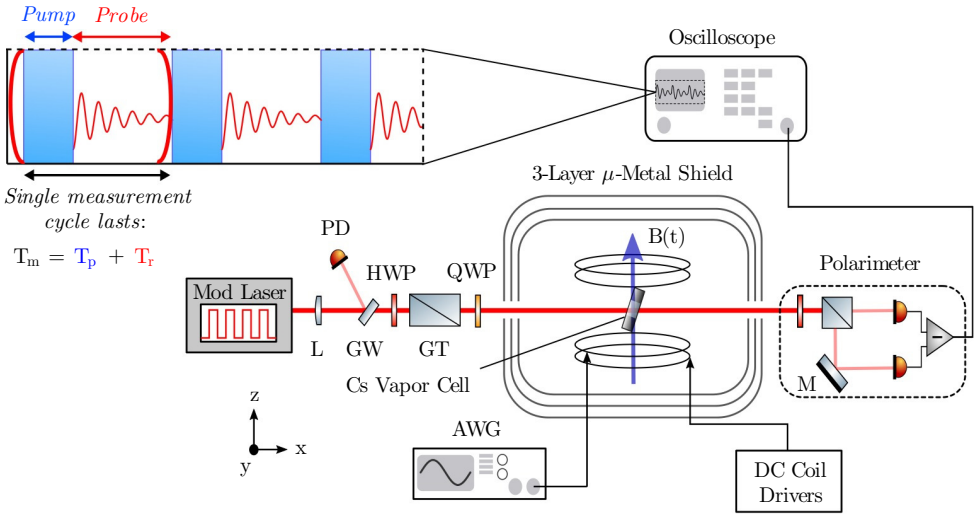

Fig. 1. Experimental set-up for an amplitude-modulated FID magnetometer with a microfabricated Cs vapor cell containing N_2 buffer gas at a pressure of 165 Torr [10]. Amplitude modulation is accomplished using the first order deflection of an acousto-optic modulator (AOM). DC and AC components of the applied time-varying magnetic fields, orthogonal to the beam axis, are generated using two independent sets of Helmholtz coils. Detection of the time-dependent optical rotation angle is performed using a balanced polarimeter and is recorded on an oscilloscope. The pump-probe sequence illustrates the sampling procedure of the FID technique. (PBS: polarising beam splitter, HWP: half-wave plate, GT: Glan-Thompson polarizer, QWP: quarter-wave plate, GW: glass window, M: mirror, L: lens, PD: photodiode.)

Optics EXPRESS

phase extending over a time T_r, so that the total single-measurement time is $T_m = 1/f_d = T_p + T_r$, where f_d is the sensor repetition rate. In a single measurement the signal $S(t)$ from the detector is recorded at a sampling rate F_s. This signal can be modelled as,

$$S(t) = gM_x(t) + \epsilon_n(t), \tag{1}$$

where g is a transduction constant, $M_x(t)$ is the projection of the spins along the probe axis, and $\epsilon_n(t)$ represents signal noise. From a single FID trace the strength of the field $|\mathbf{B}|$ averaged over T_r can be inferred by fitting the data to a model consisting of a decaying sinusoid,

$$M_x(t) = A\, e^{-\gamma_2 t} \sin(\omega_L\, t + \phi_0), \tag{2}$$

where A, γ_2, ω_L and ϕ_0, are the free-parameters of the model. From the fitted sinusoid frequency and Larmor rate (i.e. $\omega_L = 2\pi f_L = \gamma|\mathbf{B}|$, where $\gamma/2\pi = 3.5$ Hz/nT represents the gyromagnetic ratio of Cs) the strength of the field can be inferred. Alternative estimators can also be implemented, for instance the time series can be analyzed in the frequency domain; from the estimated frequency of the spectral peak and the field-dependence of the Larmor rate, the strength of the field can be inferred.

3. Experimental methods

A schematic of the experimental arrangement, consisting of an amplitude-modulated FID magnetometer, is shown in Fig. 1. The sensor head comprises of a microfabricated Cs vapor cell, the specifications of which are discussed by Hunter et al. in [10]. The intrinsic relaxation rate of the vapor cell was estimated to be $\gamma_{20} \simeq 1.5$ kHz at 85 °C based on the cell dimensions and buffer gas content [13]. A gated current is supplied to a resistive heating element to control the temperature of the vapor cell with measurements performed during the off state to avoid spurious magnetic field contributions. The alkali number density is optimized based on the signal-to-noise ratio (SNR) and transverse relaxation rate to achieve maximum magnetometer precision; further increase of the alkali density provides a way to enhance the atomic bandwidth at the expense of degraded sensitivity [12]. The vapor cell is positioned inside a three-layer μ-metal shield to reduce ambient magnetic fields to several nT and suppress technical noise contributions including line noise. Two sets of Helmholtz coils are placed inside the shield to produce a measurement field orthogonal to the beam propagation axis. The first is driven by a DC current supply (powered by a 12 V car battery) that was designed to generate a stable and uniform bias field that can surpass the Earth's magnetic field of $\sim 50\,\mu$T. The second set of coils are used for modulation purposes and consist of a single turn, with a resistor placed in series to control the range of producible magnetic fields available when driven by an arbitrary function generator (Keysight 33500B series) which has a maximum voltage of 10 V. The time constant of the RL circuit was measured to be short enough that no roll-off was observed up to the MHz range.

An extended cavity diode laser (Toptica DL pro) is manually tuned to the D_1 line using an auxiliary Cs reference cell. In our microfabricated cell the presence of N_2 buffer gas yields a broadened optical spectrum consisting of two merged peaks, with slight overlap between the groundstate resonances [10]. The laser frequency was centered on the $F = 3 \rightarrow F'$ absorption line as this can lead to superior magnetometer sensitivity due to the light narrowing phenomenon [14]. The laser beam passes through a half-wave plate and Glan-Thompson polarizer to ensure maximum transmission of linearly polarized light. A quarter-wave plate introduces a tunable degree of ellipticity into the beam before it strikes the vapor cell producing an ideal polarization for efficient optical pumping and detection in account of the single-beam geometry. The first order deflection of an acousto-optic modulator (AOM), driven by a frequency mixer, is utilized to pulse the optical power; the control voltage input is administered by the same programmable arbitrary function generator that drives the modulation coils whereas the RF input

Optics EXPRESS

is supplied by a signal generator (Marconi 2022). The dynamic optical power range of the AOM can be extended from approximately 1 μW to around 6 mW and is monitored using reflection from a glass window with a calibrated photodiode. All of our experiments employ synchronous optical pumping [6, 10] for a duration $T_p \approx 330\,\mu s$, while the probing time T_r was set according to the specific experiment as described in the sections below. The pump and probe powers were set to $P_p \approx 6$ mW and $P_r \approx 200\,\mu$W respectively, while the beam area was measured to be 2.5 mm^2. An elevated pump power is required to maximize the induced spin coherence through optical pumping. Detection of spin precession was performed using a balanced polarimeter to analyze the polarization of the transmitted light. When adequately balanced, this detection mode provides excellent noise rejection and signal enhancement as a consequence of the differential measurement. An initial transient, instigated by the difference in absorption between the two ports of the polarimeter, is typically observed at the start of each FID signal and is simply removed before processing the data. The FID traces were recorded using a Tektronix DPO5034 digital phosphor oscilloscope with 12-bit voltage resolution at a sampling rate of $F_s = 2$ MHz. Each acquired signal train is post-processed to extract the relevant free-parameters, most importantly the precession frequency of the atoms as described above. Our experiments were performed at two cell temperatures, 85°C and 100°C, and from the damped sinusoid fit the power broadened magnetic linewidths were estimated to be 2.8 kHz and 4.3 kHz, respectively.

4. Waveform reconstruction of AC magnetic signals

The magnetometer's capability at reproducing applied oscillating fields is demonstrated in Fig. 2. The repetition rate of the sensor was set to $f_d = 1$ kHz and the power broadened transverse

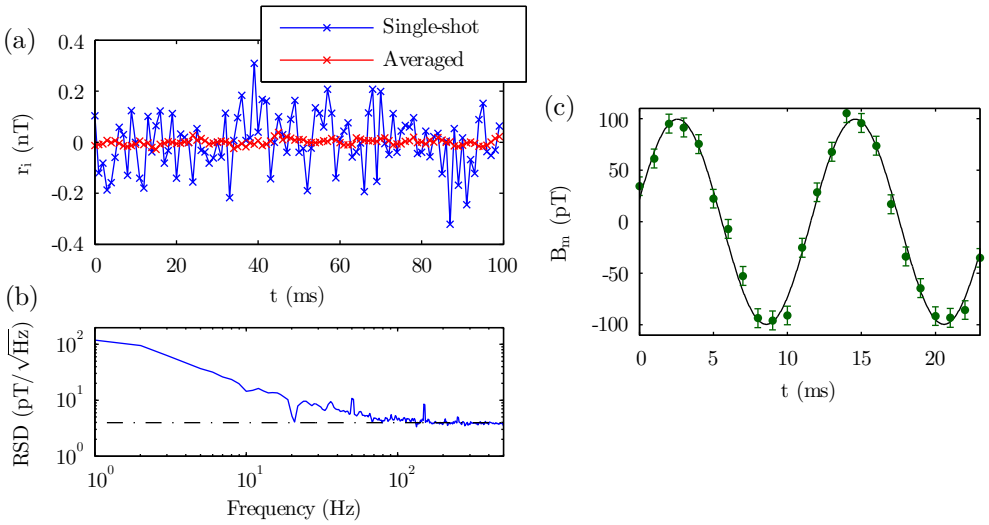

Fig. 2. (a) An applied 7 nT sinusoidal modulation oscillating at $f_m = 20$ Hz was reconstructed by the magnetometer at a repetition rate of $f_d = 1$ kHz over a period of 25 s. Fit residuals for a 100 ms portion of the reconstructed waveform (blue trace), and for a weighted average of 247 similar segments (red trace). The standard deviation of the fluctuations are 112.6 pT and 11.7 pT for the single-shot and averaged waveforms, respectively. (b) Single-shot measurement residuals, over a period of 1 s, converted to the frequency domain. The dot-dashed line is an indication of the optimum sensitivity of the device at 3.9 pT/$\sqrt{\text{Hz}}$. (c) Reconstructed waveform (208 averages) of a 100 pT magnetic field perturbation oscillating at 83.3 Hz. The standard deviation of the fit (black line) residuals was calculated to be 8.7 pT.

Optics EXPRESS

relaxation rate was close to $\gamma_2 \simeq 2.8$ kHz. The time-varying magnetic field was inferred from the Larmor frequency of subsequent FID traces in a signal train by applying the Levenberg-Marquardt algorithm to the data using the model provided in Eq. (2) [10]. The ensuing reconstructed signals were then fit to a sinusoidal model using the same algorithm. A 7 nT applied field oscillating at 20 Hz was sampled in 1 ms increments by the magnetometer over a period of 25 s. Figure 2(a) presents the residuals of the sinusoidal fit (blue trace) for 100 ms of the reproduced waveform. A weighted average was then implemented on 247 snapshots of similar 100 ms segments over $\sim$ 25 s. This averaging is possible as the frequency of the modulation field is a subharmonic of the repetition rate of the sensor. The fit residuals of the corresponding waveform (red trace) demonstrate a clear improvement in the magnetic field fluctuations observed in the time domain. This is further emphasized in Fig. 2(c) showing the signal reconstruction of a smaller 100 pT magnetic field perturbation that would otherwise have been buried in noise. The best sensitivity of the device is exhibited in Fig. 2(b) in the form of a DFT of the single-shot fit residuals over a period of 1 s. In order to smooth out the spectrum, a running average was performed over the full 25 s data set enabling features such as line noise to be observed in the spectrum. The dip occurring at 20 Hz is due to noise suppression at the modulation frequency as a consequence of the fit. The sensitivity close to the Nyquist limited bandwidth of the sensor, defined as $f_N = f_d/2$, was calculated to be 3.9 pT/$\sqrt{\text{Hz}}$. Each data point in Fig. 2(c) was an average of 208 points therefore the expected fluctuations in the residuals would be approximately 8.6 pT if one multiplies the measured sensitivity by the square root of the measurement bandwidth, calculated as $1/(208 \times 1\,\text{ms}) \simeq 4.8$ Hz. This closely resembles the measured root-mean-squared deviation of 8.7 pT.

FM can significantly distort the spectrum of a FID signal therefore one may consider using a low modulation amplitude to characterize the frequency response of the sensor. Figure 3(a) shows the peak-to-peak frequency deviation observed as the amplitude of the AC field was varied

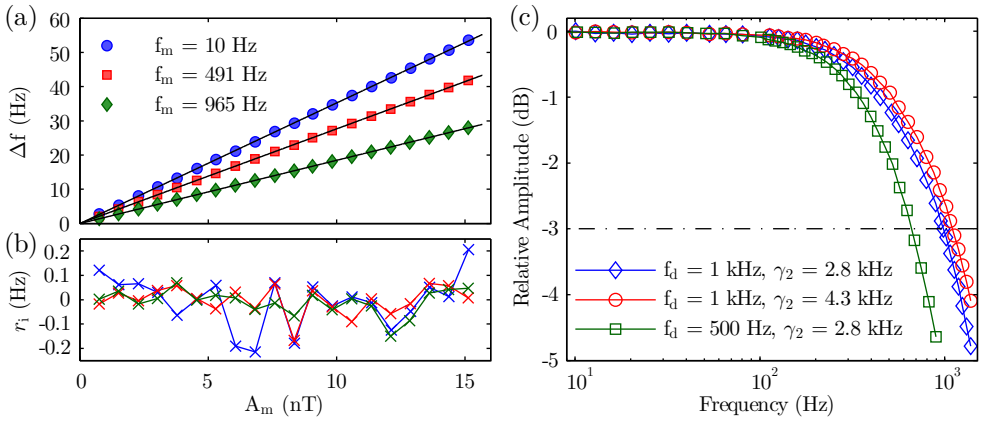

Fig. 3. (a) Linearity of the detector observed by measuring the peak-to-peak frequency deviation at a range of field modulation amplitudes using f_m = 10 Hz, f_m = 491 Hz, and f_m = 965 Hz represented by the blue, red and green data points, respectively. The solid lines are linear fits to the data. (b) Linear fit residuals. (c) Frequency response of a FID magnetometer using different experimental parameters as noted in the legend. Data points with frequencies above the Nyquist limit are folded back within the detectable bandwidth through aliasing. Interpolation has been utilized as a guide for the eye allowing extraction of the (−3 dB) bandwidths, estimated to be 671 Hz, 975 Hz and 1.1 kHz for the green, blue and red data sets, respectively. The size of the markers are larger than the corresponding error bars in both (a) and (c) and have hence been omitted.

Optics EXPRESS

using three different modulation frequencies. Oscillating frequency components beyond half the repetition rate of the magnetometer are aliased in accordance with the Nyquist theorem (see section 5). The modulation coil was calibrated using the magnetometers DC response by incrementally increasing the static magnetic field. The conversion from coil voltage to magnetic field can then be determined empirically from the straight line dependence. The absence of FM effects is highlighted by the lack of trends in the straight line fit residuals, shown in Fig. 3(b), which are several orders of magnitude smaller than the applied oscillation. The reduced gradients at higher frequencies indicate that the reconstructed signal diverges from the true waveform as a consequence of the magnetometers inherent frequency response. After appropriate scaling to magnetic field with respect to the gradient, the standard deviations were calculated to be 30.8 pT, 21.1 pT, and 27.7 pT for the $f_m = 10\,\text{Hz}$, $f_m = 491\,\text{Hz}$, and $f_m = 965\,\text{Hz}$ data sets, respectively.

A characterization of the FID magnetometers frequency response for various experimental parameters is shown in Fig. 3(c). An oscillating B-field of amplitude $A_m \simeq 7\,\text{nT}$ was administered with the modulation coils at a range of frequencies. Data was collected for different repetition and damping rates in an attempt to understand the independent effects of these experimental parameters on the frequency response of the system. As anticipated, clear attenuation of the reconstructed waveforms occur at higher frequencies as a consequence of the subtle interplay between the repetition rate and spin coherence time. Sharp discontinuities in the time domain can lead to truncation artefacts that increase the spectral linewidth of a single FID signal resulting in an enhancement of the the overall sensor bandwidth, as seen in Fig. 3(c); the data taken at $f_d = 1\,\text{kHz}$ and $\gamma_2 = 2.8\,\text{kHz}$ experienced significant truncation in comparison to the other data sets. The detection window can be thought of as a rectangular function in the time domain whose corresponding Fourier transform pair is a sinc function, therefore reducing the probing time will inevitably increase the width of the sinc function. These truncation artefacts are commonplace in FID spectra, especially in NMR measurements, and are often seen as a disadvantage in this application due to the loss in spectral resolution [15]. As well as improving the bandwidth of the sensor, signal truncation can also increase the magnetometer precision by improving the Cramer-Rao lower bound (CRLB) which is optimized at $T_r = 2/\gamma_2$ [10].

5. Technical considerations

The effects shown in Fig. 3 demonstrate that an oscillating field will cause the Larmor frequency to evolve within a single detection window, giving rise to a frequency modulated signal. This can still be adequately described by the traditional FID model with the addition of a time-dependent frequency term,

$$M_x(t) = A\, e^{-\gamma_2 t} \sin\Big(\omega_0 t + \phi_0 + \gamma \int_0^t B(\tau)\, d\tau\Big), \tag{3}$$

where $B(t)$ is the oscillating component of the magnetic signal. If we consider single tone modulation, $B(t) = A_m \cos(\omega_m t + \phi_m)$, then Eq. (3) becomes,

$$M_x(t) = A\, e^{-\gamma_2 t} \sin\big[\omega_0 t + \phi_0 + \beta \sin(\omega_m t + \phi_m)\big], \tag{4}$$

where $\beta = \gamma\, A_m/\omega_m$ is the modulation index (or depth) assuming a flat frequency response. This expression can be further simplified using the Jacobi-Anger expansion [16],

$$M_x(t) = A\, e^{-\gamma_2 t} \sum_{n=-\infty}^{\infty} J_n(\beta) \sin\big[(\omega_0 + n\omega_m)\, t + \phi_0 + n\phi_m\big], \tag{5}$$

where $J_n(\beta)$ is a Bessel function of the first kind. It can be clearly seen from Eq. (5) that multiple frequency components would begin to appear in the FID spectrum at large modulation depths.

Optics EXPRESS

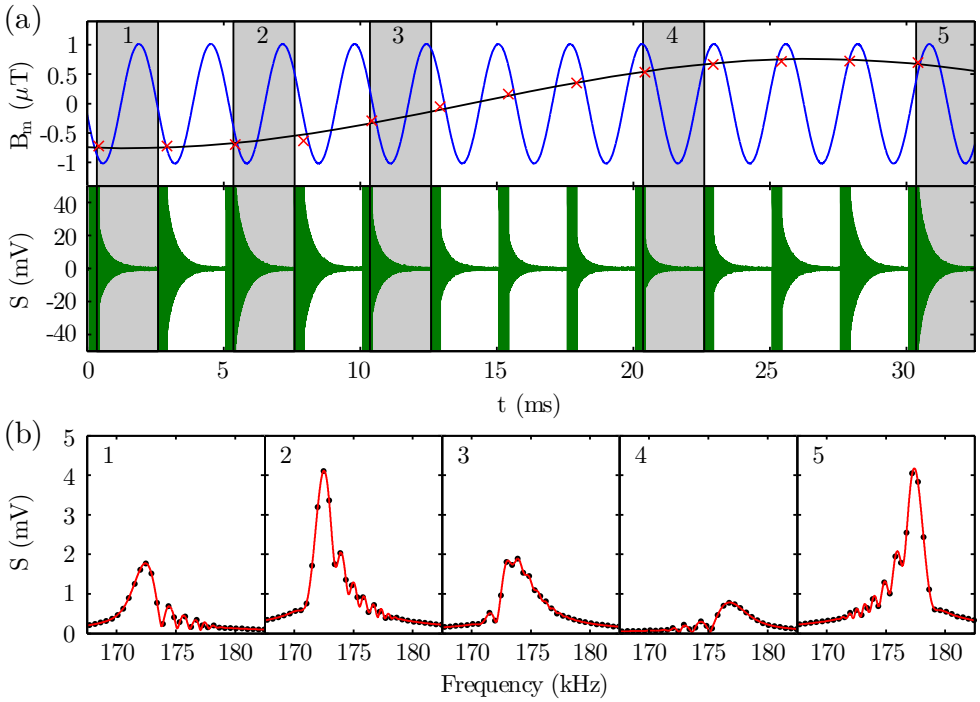

Fig. 4. (a) Top: oscillating component of the magnetic field (blue line) generated by the modulation coils, aliased reconstructed waveform (red crosses), and corresponding fit to a sinusoidal model (black line). Bottom: time series of a FID signal train (green trace). (b) Snapshots of frequency modulated FID spectra (black dots) and their associated best fits converted to the frequency domain (red lines). The numbers (top left) refer to the corresponding time-domain signals that are highlighted by a grey background.

A strong oscillating field was supplied to the modulation coils, as seen in the top plot of Fig. 4(a), that introduces distinctive FM features into the FID spectrum. Figure 4(b) shows several snapshots of the ensuing FID spectra together with their associated fits to the model described in Eq. (5). Zero-padding interpolation was applied to the spectra of the time-domain fits to enhance visualisation of the correspondence between the data and fit model in the frequency domain. The temperature of the vapor cell was 85°C and the repetition rate was set to $f_d = 400$ Hz allowing the spin polarization to fully equilibrate. Almost a full oscillation occurs within a single FID cycle giving rise to an aliased waveform if one tracks the frequency of the spectral peak, as evidenced by Fig. 4(a). This is a common feature of data acquisition systems and is typically rectified with the application of an anti-aliasing filter to eliminate these high frequency components; this is not an ideal solution for the FID magnetometer as the precession signal would also be attenuated. In fact, the true frequency of an aliased waveform can be inferred by adjusting the repetition rate slightly and observing the frequency variation in the reconstructed signal. It can also be noticed that even at these high modulation depths the correlation between the actual and reconstructed signal amplitudes are relatively close when considering the sensors frequency response. These high frequency oscillations will cause the lineshape of the FID spectra to be contingent on the phase of the respective magnetic signal. For example, the sharp initial change in magnetic field experienced by the magnetometer (see snapshot 4) leads to a larger spread in frequencies and dramatically reduced FID amplitude. This is a consequence of the magnetic field measurement being weighted by signal damping, placing emphasis on the initial portion of the FID signal.

Optics EXPRESS

Introducing such complexity into the FID spectrum will inevitably increase the difficulty of the magnetometer readout process especially if multiple sidebands share similar amplitudes (see snapshot 3). The model in Eq. (5) therefore provides an understanding of the sensors capabilities in accurately reconstructing an AC magnetic signal.

6. Conclusion and outlook

Waveform tracking of oscillating magnetic signals was demonstrated using a magnetometer based on FID, employing a 1.5 mm thick Cs vapor cell with relaxation rates on the order of kHz. The pulsed technique polarizes the atomic sample during the optical pumping phase; the precessing spins are then detected through optical rotation of the transmitted light for a finite readout period. Excellent reconstruction of a sinusoidal waveform oscillating at 20 Hz was performed using a repetition rate, f_d = 1 kHz, with the atomic spins depolarizing at a rate, γ_2 = 2.8 kHz. The impressive sensitivity of the magnetometer was also demonstrated by reproducing a 100 pT modulation using signal averaging. The frequency response of the sensor was investigated in detail for various repetition and decoherence rates. It was discovered that the bandwidth of the sensor can be extended through signal truncation which can also enhance the precision of frequency extraction in accordance with the minimized CRLB condition. Additional improvements in sensor bandwidth are gained by raising the transverse relaxation rate through mechanisms such as spin-exchange collisions or power broadening, however, this will also degrade the sensitivity. A high amplitude magnetic signal was utilized, introducing FM effects into the FID spectrum; a model describing the corresponding behavior was developed using Bessel functions of the first kind. Aliased components also materialized for applied oscillations that surpassed the Nyquist limited bandwidth, with the frequency of the aliased waveform dependent on the repetition rate of the sensor.

With sensitivities at the single-pT level, this novel approach to signal reconstruction provides reliable and accurate detection of weak oscillating fields. There are clear and obvious limitations in extracting broad spectral information from a periodic measurement. This study served to provide an exploration of the devices capabilities with the simplest case of a discrete spectrum. The magnetometer has the ability to detect a superposition of different discrete frequencies or signals with broad continuous spectra, as long as the frequencies of interest reside within the Nyquist limited bandwidth; however, one must be careful to apply an appropriate anti-aliasing filter, post-acquisition, to avoid signal distortion. This has been achieved experimentally in an unshielded environment in which the multiple harmonics contained in noise from the power lines and surrounding laboratory equipment were detected. The design simplicity, scalability and all-optical nature of this implementation is attractive for numerous applications, such as magnetocardiography (MCG) where the sensor requires a flat response within the desired frequency range. For applications such as MCG where magnetic source localization is required and hence sensor networks are beneficial, the FID technique benefits from minimal cross-talk due to the absence of rf coils.

The data presented in this paper are available from the University of Strathclyde data archive [17].

Funding

Engineering and Physical Sciences Research Council (EPSRC); Texas Instruments Incorporated (TI).

Acknowledgments

D. H. acknowledges project funding from EPSRC through the CDT in applied photonics programme. He also acknowledges Texas Instruments for their funding and involvement in the

Optics EXPRESS

project. D. H. would like to thank Dr. Stuart Ingleby, Dr. Paul Griffin and Dr. Jonathan Pritchard for many valuable discussions.

Disclosures

The authors declare that there are no conflicts of interest related to this article.

References

1. D. Budker and D. F. J. Kimball, *Optical magnetometry* (Cambridge University, 2013).
2. J. Kitching, S. Knappe, V. Shah, P. Schwindt, C. Griffith, R. Jimenez, J. Preusser, L.-A. Liew, and J. Moreland, "Microfabricated atomic magnetometers and applications," in *Frequency Control Symposium, 2008 IEEE International,* (IEEE, 2008), pp. 789–794.
3. L. Marmugi, L. Gori, S. Hussain, C. Deans, and F. Renzoni, "Remote detection of rotating machinery with a portable atomic magnetometer," Appl. optics **56**, 743–749 (2017).
4. H. Xia, A. Ben-Amar Baranga, D. Hoffman, and M. Romalis, "Magnetoencephalography with an atomic magnetometer," Appl. Phys. Lett. **89**, 211104 (2006).
5. S. Groeger, G. Bison, P. E. Knowles, R. Wynands, and A. Weis, "Laser-pumped cesium magnetometers for high-resolution medical and fundamental research," Sens. Actuator A-Phys. **129**, 1–5 (2006).
6. Z. D. Grujić, P. A. Koss, G. Bison, and A. Weis, "A sensitive and accurate atomic magnetometer based on free spin precession," The Eur. Phys. J. D **69**, 135 (2015).
7. D. Sheng, S. Li, N. Dural, and M. Romalis, "Subfemtotesla scalar atomic magnetometry using multipass cells," Phys. review letters **110**, 160802 (2013).
8. S. Afach, G. Ban, G. Bison, K. Bodek, Z. Chowdhuri, Z. D. Grujić, L. Hayen, V. Hélaine, M. Kasprzak, K. Kirch, P. Knowles, H.-C. Koch, S. Komposch, A. Kozela, J. Krempel, B. Lauss, T. Lefort, Y. Lemière, A. Mtchedlishvili, O. Naviliat-Cuncic, F. M. Piegsa, P. N. Prashanth, G. Quéméner, M. Rawlik, D. Ries, S. Roccia, D. Rozpedzik, P. Schmidt-Wellenburg, N. Severjins, A. Weis, E. Wursten, G. Wyszynski, J. Zejma, and G. Zsigmond, "Highly stable atomic vector magnetometer based on free spin precession," Opt. Express **23**, 22108–22115 (2015).
9. S. Afach, C. A. Baker, G. Ban, G. Bison, K. Bodek, Z. Chowdhuri, M. Daum, M. Fertl, B. Franke, P. Geltenbort, K. Green, M. G. D. van der Grinten, Z. Grujic, P. G. Harris, W. Heil, V. Hélaine, R. Henneck, M. Horras, P. Iaydjiev, S. N. Ivanov, M. Kasprzak, Y. Kermaïdic, K. Kirch, P. Knowles, H.-C. Koch, S. Komposch, A. Kozela, J. Krempel, B. Lauss, T. Lefort, Y. Lemière, A. Mtchedlishvili, O. Naviliat-Cuncic, J. M. Pendlebury, F. M. Piegsa, G. Pignol, P. N. Prashant, G. Quéméner, D. Rebreyend, D. Ries, S. Roccia, P. Schmidt-Wellenburg, N. Severijns, A. Weis, E. Wursten, G. Wyszynski, J. Zejma, J. Zenner, and G. Zsigmond, "Measurement of a false electric dipole moment signal from 199 Hg atoms exposed to an inhomogeneous magnetic field," The Eur. Phys. J. D **69**, 225 (2015).
10. D. Hunter, S. Piccolomo, J. Pritchard, N. Brockie, T. Dyer, and E. Riis, "Free-induction-decay magnetometer based on a microfabricated Cs vapor cell," Phys. Rev. Appl. **10**, 014002 (2018).
11. R. Jiménez-Martínez, W. C. Griffith, Y.-J. Wang, S. Knappe, J. Kitching, K. Smith, and M. D. Prouty, "Sensitivity comparison of Mx and frequency-modulated Bell–Bloom Cs magnetometers in a microfabricated cell," IEEE Trans. Instrum. Meas. **59**, 372–378 (2010).
12. R. Jiménez-Martínez, W. C. Griffith, S. Knappe, J. Kitching, and M. Prouty, "High-bandwidth optical magnetometer," JOSA B **29**, 3398–3403 (2012).
13. T. Scholtes, S. Woetzel, R. IJsselsteijn, V. Schultze, and H.-G. Meyer, "Intrinsic relaxation rates of polarized Cs vapor in miniaturized cells," Appl. Phys. B **117**, 211–218 (2014).
14. T. Scholtes, V. Schultze, R. IJsselsteijn, S. Woetzel, and H.-G. Meyer, "Light-narrowed optically pumped Mx magnetometer with a miniaturized Cs cell," Phys. Rev. A **84**, 043416 (2011).
15. N. E. Jacobsen, *NMR spectroscopy explained: simplified theory, applications and examples for organic chemistry and structural biology* (John Wiley & Sons, 2007).
16. H. Korsch, A. Klumpp, and D. Witthaut, "On two-dimensional Bessel functions," J. Phys. A: Math. Gen. **39**, 14947 (2006).
17. D. Hunter, R. Jiménez-Martínez, J. Herbsommer, S. Ramaswamy, W. Li, and E. Riis, Data for: "Waveform reconstruction with a Cs based free-induction-decay magnetometer", University of Strathclyde, https://doi.org/10.15129/61312697-3649-4655-bbc8-91cf1afebb14 (2018).